REAL-TIME, REAL-SPACE DENSITY FUNCTIONAL THEORY CALCULATIONS OF ELECTRON SCATTERING IN MATERIALS

By

Benjamin Wyatt

Honors Thesis

Submitted to the Faculty of the

Department of Physics and Astronomy of Vanderbilt University

in partial fulfillment of the requirements

for

DEPARTMENTAL HONORS

in

Physics

April, 2012

Nashville, Tennessee

Primary Advisor:

Dr. Kalman Varga

Committee of Examiners:

Dr. Norman Tolk

Dr. Paul Sheldon

Dr. Charles Brau

TABLE OF CONTENTS

Abstract:

Density functional theory is utilized in real-time, real-space simulations of LEED measurements and attosecond electron scattering. For LEED measurements, we find that our simulation results agree well with experimental data and other theoretical approaches. For attosecond electron scattering, we find that the wavefunction of the scattered electron is not signficantly changed by the scattering process, and the measured electron density seems to be related to the initial form of the wave-packet. However, further investigation is needed to confirm these results for different choices of initial form.

CHAPTER I

Introduction

1.1 Context and Motivation for Work

Electrons have become indispensable tools for imaging atomic, molecular, and crystal geometries. In particular, low-energy electron diffraction (LEED) is a ubiquitious and exceptionally useful method for analyzing the atomic structures of various materials [1]. In LEED, a collimated electron beam with an electron energy of $E = 20 - 200$ eV is fired at the surface of a crystalline material. The electrons are either reflected or transmitted through the material and impact on a phosphor screen. Due to their interaction with the crystal lattice, the electrons will form a diffraction pattern on the detector, which can then be analyzed to determine key properties of the atomic surface. Proper interpretation of LEED measurements requires accurate computational simulation of the surface under investigation [2]. Since an individual electron will almost certainly encounter multiple atoms in the crystalline material, a LEED measurement must presume that the electron undergoes a complex multiple

scattering process. As such, the relationship between the observed diffraction pattern and the atomic structure of the material may be very complex, and accurate computer simulations can do much to clarify this relationship for experimentalists and theorists. Current computational approaches to electron diffraction (primarily the Bloch wave method [3] and multislice theory [4]) leave much to be desired for LEED applications. The Bloch wave method is typically used for transmission electron microscopy (TEM) measurements [3], and therefore deals with electrons of much higher kinetic energy ($E = 100 - 300$ keV). It yields accurate results in this regime, but is limited to very small simulation volumes, making it impractical for studying larger systems. The multislice approximation, also primarily developed for TEM applications, fares reasonably well for larger simulation volumes, but it assumes that the kinetic energy of the incident electron is much greater than the potentials experienced inside the sample, and this is highly questionable for electrons in the LEED energy range [5]. Moreover, the multislice approach must repeat its computation for each desired electron energy, making it less computationally efficient.

In the present work, we present a unified theoretical and computational framework to investigate electron diffraction in solids. This approach has several advantages. First, it treats high- and low-energy electrons on an equal footing, and is therefore equally applicable to LEED and TEM measurements, although here we focus on LEED applications. Second, unlike multislice theory, our approach can extract data for the entire range of desired electron energies in a single computation; no repetition is required. Third, our approach propagates electrons in real time (unlike multislice approaches, which typically work in the energy domain) and real space (unlike Bloch

approaches, which typically work in reciprocal space). This intuitive approach, if not a computational advantage, is certainly an intellectual and pedagogical benefit; if the purpose of computational physics is to provide new insight into physical systems, then it is reasonable that approaches that mimic experiment as closely as possible might prove particularly valuable in generating these insights.

Beyond conventional applications of electron imaging of atomic structures, the advent of attosecond electron technology promises new and exciting tools for the study electron dynamics in materials. An attosecond electron pulse can be conveniently defined by reference to the Heisenberg uncertainty principle [6]. That is, if $\Delta E \Delta t \geq \frac{\hbar}{2}$, then an attosecond electron pulse has a Δt in the attosecond regime. Δt can be thought of as the time required for the electron wavefunction to pass by a point in space, and is therefore a useful way to characterize the maximum possible temporal resolution of electron imaging techniques. Thus attosecond electron pulses have ideal temporal (<1 fs) and spatial ($\sim$ Å) resolution for imaging electron dynamics in atoms [6]. This has led to proposals to perform so-called "4D" diffraction and microscopy measurements, e.g., high-resolution movies of electron dynamics, using attosecond electron pulses [7]. Attosecond electron wave pulses have already found applications in interferometry measurements [8], electron holography [9], measurements of nuclear motion [10], and imaging of atomic and molecular orbitals [11], among others. However, as with LEED measurements, accurate computer simulations will be necessary for a full understanding of attosecond electron diffraction, and at present there is a lacuna of such simulations.

The present work aims to fill this gap by extending the real-time, real-space com-

putational strategy used for LEED measurements to describe attosecond electron pulse scattering from atoms and molecules. The ultimate goal of these simulations is 4D imaging of electron diffraction. These movies can be used both as an aid for experimental efforts to perform 4D electron diffraction experiments and a way to test the validity of our theoretical assumptions as they are applied to different systems.

1.2 Outline of the Work

The organization of this thesis is as follows: first, we present our real-time, real-space computational approach with specific reference to our LEED simulations. We then describe our main theoretical tool, density functional theory (DFT). Next, we discuss the results of our LEED simulations and assess the utility of our approach. We then present our approach to attosecond electron scattering; since our method is somewhat similar to our approach to LEED, we mainly take note of the differences between the two approaches. We then present the results of our scattering simulations, followed by some concluding remarks.

CHAPTER II

Real-Time, Real-Space Calculations

Our theoretical approach begins by describing electrons as wave-packets. This description has many advantages over alternative models, such as the plane wave description. Gaussian wave-packet parameters allow us to fine-tune the width of our wave-packets in all three spatial dimensions, which facilitates the simulation of finite-size effects of an electron source. This description also allows us to extract information about the phases and amplitudes of the component eigenfunctions of the wave-packet. Furthermore, propagation of wave-packets in the time domain can yield eigenfunctions of arbitrary nanostructures, making the wave-packet description particularly valuable to computational nanoscience [12].

Our approach propagates electrons in real time and real space. However, since a computer can only hold a discrete number of values, we cannot sample the electron wavefunction across a continuum. Instead, we measure our electron on a discretized

grid, where neighboring points in space are separated by a distance d, and the wave-packet's time evolution is sampled at some regular interval Δt. There is a tradeoff between computational efficiency and accuracy; smaller choices of d and Δt yield more accurate results, but calculations become more costly. Our choices for these parameters are discussed below.

In our LEED simulations, we need only consider the scattering of single electrons, as the time between electron pulses ($\sim 10^{-9}$ s) is much greater than the characteristic time of the scattering interaction ($\sim 10^{-15}$ s). We begin with the usual time-dependent Schrödinger equation for an electron wavefunction $\Phi(\mathbf{r}, t)$:

$$i\hbar \frac{\partial \Phi(\mathbf{r}, t)}{\partial t} = H\Phi(\mathbf{r}, t) = \left[-\frac{\hbar^2}{2m}\nabla^2 + V(\mathbf{r}) \right] \Phi(\mathbf{r}, t). \tag{2.1}$$

$V(\mathbf{r})$ is the effective potential of the crystal film, which is considered to be frozen for the duration of the scattering process. In the case of an electron with initial (average) kinetic energy $E_0 = \hbar^2 k_0^2 / 2m$ and momentum $p_0 = \hbar k_0$, we may write the initial wave-function as

$$\Phi(\mathbf{r}, t = 0) = e^{ik_0 z} \phi_g(\mathbf{r}, 0), \tag{2.2}$$

where $\phi_g(\mathbf{r}, 0)$ the initial Gaussian distribution of the wave-packet. This constrains $\phi_g(\mathbf{r}, 0)$ to a form that is easy to implement in real space, easing our computational task. Although this is not explored in the present work, expressing the wavefunction in this manner also allows for the successful simulation of high-energy electrons ($E > 100$ keV) [13].

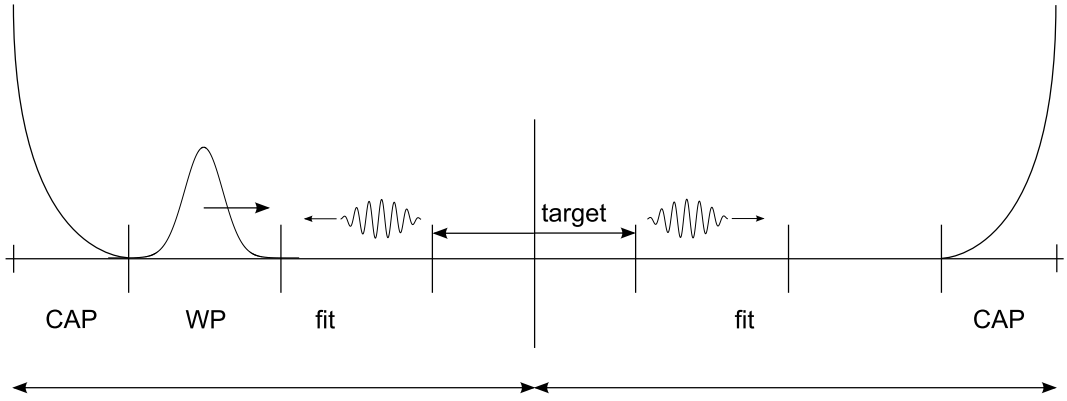

Figure 2.1: Schematic illustration of wave packet propagation. The electron wave-packet is propagated in time through the grid until it is absorbed the CAPs at either end of the grid. The time evolution of the wave-packet is then known, and we fit it to known asymptotic forms in the regions to the left and right of the sample. This figure is reproduced from Ref. [13]

Our computational setup is schematically illustrated in Fig. 2.1. We begin with a wave-packet far away (e.g., sufficiently far that the wavefunctions of the electron and sample to do not interact appreciably with one another) from the target crystal, and propagate the electron in time using the normal exponential term:

$$\Phi(\mathbf{r}, t + \Delta t) = e^{-iH\Delta t/\hbar}\Phi(\mathbf{r}, t). \tag{2.3}$$

This allows us to propagate the Gaussian wave-packet throughout the entire simulation box. However, the exponential term cannot be handled directly due to the Hamiltonian operator, so we must approximate it in order to carry out our calculation. Here, we choose to expand the exponential using a Taylor series:

$$e^{-iH\Delta t/\hbar} \approx \sum_{n=0}^{N} \frac{(\frac{-i\Delta t H}{\hbar})^n}{n!}. \tag{2.4}$$

This is a simple and popular method for approximating the exponential operator. Its only disadvantage is that it is unstable for large time steps, which forces us to use relatively small values of Δt in our computation. For the present approach, however, this requirement is not problematic, and we can find appropriate values of Δt that allow for both reasonable computation times and successful time development of the wavepacket.

The time propagation of the wavepacket, however, raises a concern common to numerical grid approaches. Since we require that the electron wavefunction approach zero at the boundaries of the simulation box, we will encounter unphysical reflection effects as the electron approaches the boundary. In order to avoid these effects, we implement a complex absorbing potential (CAP)[14, 15] of the form $V = V_0(\mathbf{r}) + iW(\mathbf{r})$, where V_0 is the original (real-valued) potential of our system, and W is an arbitrary function that is chosen to be non-zero only near the boundaries of the simulation box. The CAP is usually designed to go to infinity at the simulation box in order to totally eliminate undesirable reflections. It can easily be shown that this complex absorbing potential forces the electron wavefunction to vanish in the asymptotic regions of the box [16], but does not affect the wavefunction near the scattering region, where our measurements are made.

With these two difficulties solved, only one more problem confronts our computational approach: computation of the second derivative of the electron wavefunction. This is necessary to calculate the Hamiltonian of our system, yet it is not immediately obvious how a second derivative should be approximated for a series of discrete points, rather than for a continuous function. We solve this dilemma via the approach

of Ref. [17]: a finite difference approach that approximates $\frac{d^2\Phi}{dx^2}$ using the values of the wavefunction at neighboring points. For our five-point finite difference approximation, we can expand any function $\phi(x \pm 2d)$, where d is the spacing between grid points in the x-direction, as:

$$\phi(x \pm 2d) = \phi(x) \pm \phi'(x)2d + \frac{1}{2}\phi''(x)(2d)^2 \pm \frac{1}{6}\phi'''(x)(2d)^3 + \frac{1}{1}24\phi''''(x)(2d)^4, \quad (2.5)$$

where ϕ' is the first derivative, ϕ'' is the second derivative, etc. We can write down a similar equation for $\phi(x \pm h)$. This, coupled with the identity $\phi(x) = \phi(x)$, creates a linear system of equations that can be solved for ϕ'':

$$\phi''(x) = -\frac{1}{12}[\phi(x+2d) + \phi(x-2d)] + \frac{4}{3}[\phi(x+d) + \phi(x-d)] - \frac{5}{2}\phi(x). \quad (2.6)$$

This centered method, so called due to its symmetry about x, produces a well-defined second derivative for all points in the grid except for those within $2d$ of the grid boundary. For these points, we use a forward approach, which results in a similar formula that incorporates $\phi(x+3d)$ and $\phi(x+4d)$, but not $\phi(x-d)$ or $\phi(x-2d)$. With these formulae in hand, we are well-positioned to compute the second derivative, and hence to solve the scattering problem using our numerical grid approach. All that remains is to extract the transmission and reflection coefficients from the information contained in the time-developed wavefunctions. Once the time evolution of the Gaussian wave-packet is completed, we use a Fourier transform to move from the time domain

to the energy domain:

$$\Phi(x,E) = \frac{1}{2\pi}\int \Phi(x,t)e^{iEt/\hbar}dt. \tag{2.7}$$

For the case of a thin film, where transmission and reflection are both possible, the wavefunction in the asymptotic regions (e.g., those to the far left and far right of the sample) can be expressed as:

$$\Phi(\mathbf{r},E) = \begin{cases} e^{i\mathbf{k_{0\parallel}}\cdot\rho}e^{i\mathbf{k_{0\perp}}x} + \sum_{\mathbf{g}} R_{\mathbf{k_{0\perp}g}}e^{i(\mathbf{k_{0\parallel}}+\mathbf{g})\cdot\rho}e^{-i\mathbf{k}^{-}_{\mathbf{g}\perp}x)} & x\to-\infty \\ \sum_{\mathbf{g}} T_{\mathbf{k_{0\perp}g}}e^{i(\mathbf{k_{0\parallel}}+\mathbf{g})\cdot\rho}e^{i\mathbf{k}^{+}_{\mathbf{g}\perp}x} & x\to+\infty, \end{cases} \tag{2.8}$$

where $\rho = (x,y)$, and $\mathbf{g}$ is the reciprocal lattice vector of the crystal. In the case of a bulk film, however, the transmission probability is zero, and the asymptotic form is reduced to:

$$\Phi(\mathbf{r},E) = e^{i\mathbf{k_{0\parallel}}\cdot\rho}e^{i\mathbf{k_{0\perp}}x} + \sum_{\mathbf{g}} R_{\mathbf{k_{0\perp}g}}e^{i(\mathbf{k_{0\parallel}}+\mathbf{g})\cdot\rho}e^{-i\mathbf{k}^{-}_{\mathbf{g}\perp}x)}, x\to-\infty \tag{2.9}$$

We then fit our time-propagated wavefunction $\Phi(\mathbf{r},E)$ to these asymptotic forms, and use this information to extract the transmission and reflection coefficients for a given energy. The details of this extraction process are presented in Appendix A. All calculations are implemented using our own computer code.

CHAPTER III

Density Functional Theory

With the problem of propagating the electron wave-packet solved, we now turn to the other challenge of our computational task: the interaction of this wave-packet with our target. Whether this target is the surface of a crystalline material (as in LEED) or an atom or molecule (as in our attosecond electron simulations), we are confronted with a multi-electron system. The behavior of such systems is often notoriously difficult to describe. In this work, we use density functional theory (DFT) in order to study these complex systems. DFT is one of the most popular computational approaches to solving such systems due to its moderate computational cost and applicability to relatively large quantum systems. We begin with the Schrödinger equation for a system of N electrons (assuming, as per the Born-Oppenheimer Approximation, that the nuclei can be treated as stationary):

$$\left[-\sum_{i=1}^{N}\frac{\hbar^2}{2m}\nabla_i^2+\sum_{i=1}^{N}V(\mathbf{r}_i)+\sum_{i<j}^{N}U(\mathbf{r}_i,\mathbf{r}_j)\right]\Psi=E\Psi. \tag{3.1}$$

Here, $\Psi = \Psi(\mathbf{r}_1, \mathbf{r}_2, ..., \mathbf{r}_N)$ is the many-particle wavefunction. $V(\mathbf{r}_i) = \sum_{A=1}^{N} \frac{Z_A e^2}{|\mathbf{r}_i - \mathbf{R}_A|}$ is the potential felt by each electron due to the atomic nuclei of the system, where N is the number of atoms in the system, and Z_A and $\mathbf{R}_A$ are the charge and coordinate vector, respectively, of the A^{th} nucleus. $U(\mathbf{r}_i, \mathbf{r}_j) = \frac{e^2}{|\mathbf{r}_j - \mathbf{r}_i|}$ is the potential due to electron-electron interactions. The main idea of DFT is to replace the many-particle wavefunction with the electron density:

$$\rho(\mathbf{r}) = \int \Psi^*(\mathbf{r}_1, \mathbf{r}_2, ..., \mathbf{r}_N)\Psi(\mathbf{r}_1, \mathbf{r}_2, ..., \mathbf{r}_N) d\mathbf{r}_2, d\mathbf{r}_3 ... d\mathbf{r}_N. \tag{3.2}$$

This substitution is made possible by two consequences of the Hohenberg-Kohn theorems that underly DFT [18]. First, it can be shown that the electron density uniquely determines the potential of a system, and hence all its physical properties. Second, the energy functional, defined as $E(n) = F[n] + \int V(\mathbf{r}) n(\mathbf{r})$, where $n = N\rho(\mathbf{r})$, and $F[n]$ is some universal functional (e.g., it does not have an explicit dependence on $V(\mathbf{r})$), is minimized by the true electron density of the system. Taken together, these two consequences ensure that the mapping from $\Psi(\mathbf{r}_1, \mathbf{r}_2, ..., \mathbf{r}_N)$ to $\rho(\mathbf{r})$ is one-to-one, and therefore we can analyze any system in terms of the density, rather than the many-particle wavefunction. This reduces a generally intractable problem of N interacting particles with 3N spatial variables to the tractable problem of fictitious, noninteracting particles under the influence of some effective external potential. Before proceeding, we divide the energy functional into several component functionals:

$$E[n] = T_{KS}[n] + E_H[n] + E_{ext}[n] + E_{xc}[n], \tag{3.3}$$

where T_{KS} is the kinetic energy operator, $E_H = \int\int \frac{n(\mathbf{r})n(\mathbf{r}')}{|\mathbf{r}-\mathbf{r}'|} d\mathbf{r}d\mathbf{r}'$ is known as the Hartree energy, and represents the (classical) electrostatic interaction energy, $E_{ext}[n] = \int \epsilon_{ext}(\mathbf{r})n(\mathbf{r})d\mathbf{r}$ is the external energy due to fixed ions or external electric fields, and E_{xc} is the exchange correlation energy, which accounts for electron-electron interactions. This division leads to a new form of the Schrödinger equation, usually referred to as the Kohn-Sham equation:

$$\left(-\frac{\hbar^2}{2m}\nabla_i^2 + V_H[n(\mathbf{r})] + V_{ext}[n(\mathbf{r})] + V_{xc}[n(\mathbf{r})]\right)\phi_k(\mathbf{r}) = E_k\phi_k. \tag{3.4}$$

Here ϕ_k is a Kohn-Sham orbital, and we can construct $n(\mathbf{r})$ using combinations of these orbitals. Unfortunately, the Kohn-Sham equations must be solved self-consistently, as there is no way to calculate $n(r)$ directly. Our method, then, is as follows: we begin with an initial guess for $n(r)$ based on the system under observation. For example, we might approximate the electron density of an atom by a Gaussian distribution. This allows us to compute $V[n]$, which in turn allows us to define the Hamiltonian. Since we have already replaced the real electrons of the system with ficitious, noninteracting electrons, the Hamiltonian matrix of the system is relatively easy to diagonalize; the lack of electron-electron interactions ensures that most of the off-diagonal elements will be zero. This approximation is justified by the fact that the potential of the system is uniquely determined by the electron density; as long as we demand that $n(r)$ of our system of noninteracting electrons matches $n(r)$ for the system of real electrons, we are guaranteed to reproduce the Hamiltonian. Once the Hamiltonian is diagonalized, we can easily find the eigenvectors of

this Hamiltonian, which are the Kohn-Sham orbitals ϕ_k. Of course, at this point we have only a guess for $n(r)$, and therefore the Hamiltonian and its eigenvectors are at best rough approximations. However, we find that when we sum the norm of the Kohn-Sham orbitals, we obtain a new value for the electron density:

$$n_{new}(\mathbf{r}) = \sum_{k=1}^{N} |\phi_k|^2. \tag{3.5}$$

We use this new electron density to generate a new Hamiltonian, and the Kohn-Sham equation is solved again for a new electron density. This procedure is iterated until the electron density converges. Once convergence is attained, we can claim that the Kohn-Sham equations have been solved, and we obtain a good approximation of the ground-state electron density of the system under study. We also use this approach to calculate the excited states of a system, as it is simply a matter of calculating additional Kohn-Sham orbitals via Eq. (3.4) and then placing electrons into the appropriate orbitals. Since these states are not stable, we use time-dependent density functional theory (TDDFT) to describe their evolution over time. While TDDFT is more computationally difficult than DFT, the basic motivation and theoretical strategy is similar to what has already been described. The additional complications are due only to the time-dependence of the electron density functional.

The most difficult aspect of our procedure is the calculation of the exchange correlation energy, E_{xc}, which cannot be known precisely except for the case of a uniform electron gas. Here, we make the local density approximation (LDA), which is as follows: first, we determine $n(r)$ at some given point on the simulation grid.

We can then define a uniform electron gas with the same density, which will have an associated energy $\epsilon_{xc}[n]$. We then assign this energy to the grid point in question and repeat the procedure for all points in the simulation box. The electron density at neighboring points is not taken into consideration. While this approximation might seem crude, the requirement that the electron density of the gas match that of the point is normally enough to assure acceptable answers [18]. To obtain the total exchange-correlation energy, we integrate over the entire box:

$$E_{xc}[n] = \int \epsilon_{xc}(n) n(\mathbf{r}) d\mathbf{r} \tag{3.6}$$

This integral is calculated using the 3D trapezoidal rule.

One further approximation is worthy of mention. It is usually prohibitively expensive to perform computational simulations that incorporate both the inner shell and valence electrons of an atom, since valence orbitals tend to be far more spatially extended than inner shell orbitals. As such, we replace the inner-shell electrons with an appropriate pseudopotential. Specific choices of pseudopotentials are discussed in the results.

CHAPTER IV

LEED: Results and Discussion

Armed with these theoretical tools, we are now prepared to discuss the results of our computational approach to LEED measurements. In Fig. 4.1, we present our calculated transmission and reflection coefficients of graphene for typical LEED energies. It is particularly noteworthy that we find very high transmission rates from 40-200 eV, suggesting the utility of graphene for low-electron point source (LEEPS) microscopy [19] applications. Our result is in good agreement with a recent LEEPS measurement [20].

Next, we present our calculations of the LEED beam intensity through a diamond(111) 1×1 surface. In our code, we approximate this surface as a few layers of a crystal slab. We then increase the number of layers in the crystal slab until our results converge; for the present system, convergence occurred for about 15 layers. A screened Thomas-Fermi potential [21] is used to approximate the carbon atomic potentials, and we then use DFT calculations to generate an effective potential for the whole slab. The usual choice of pseudopotential for similar systems is the muffin-tin

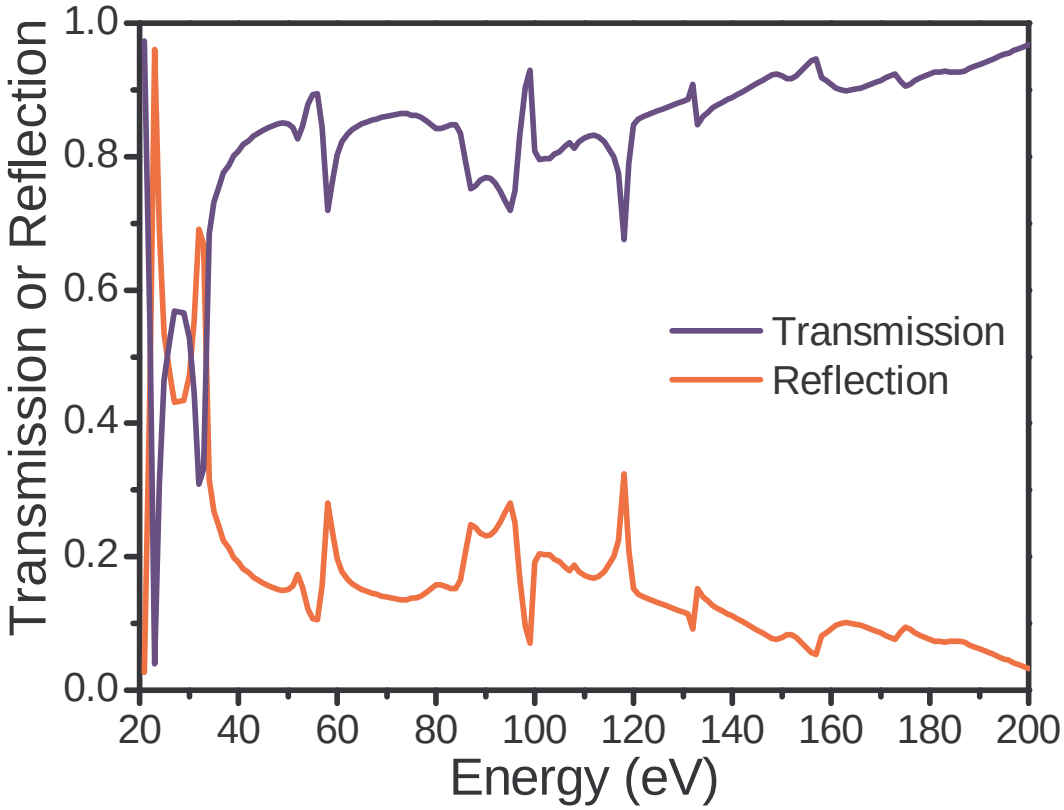

Figure 4.1: Transmission and reflection coefficients of graphene for a typical LEED energy range. This figure is reproduced from Ref. [13].

potential [22, 23] coupled with a uniform imaginary potential to account for inelastic processes. The Thomas-Fermi potential treats the interstitial regions between atoms more accurately than the muffin-tin (which assumes the potential to be constant in these regions). A comparison of our approach and a muffin-tin calculation is presented in Fig. 4.2. The muffin-tin calculation is taken from Ref. [24]. In general, the two methods agree quite well, and the different choices for carbon pseudopotentials seems to account for the small discrepancies.

Finally, we report on simulated electron diffraction patterns generated by a graphene lattice. The graphene lattice and grid schematic are shown in Fig. 4.3. Figures 4.4 and

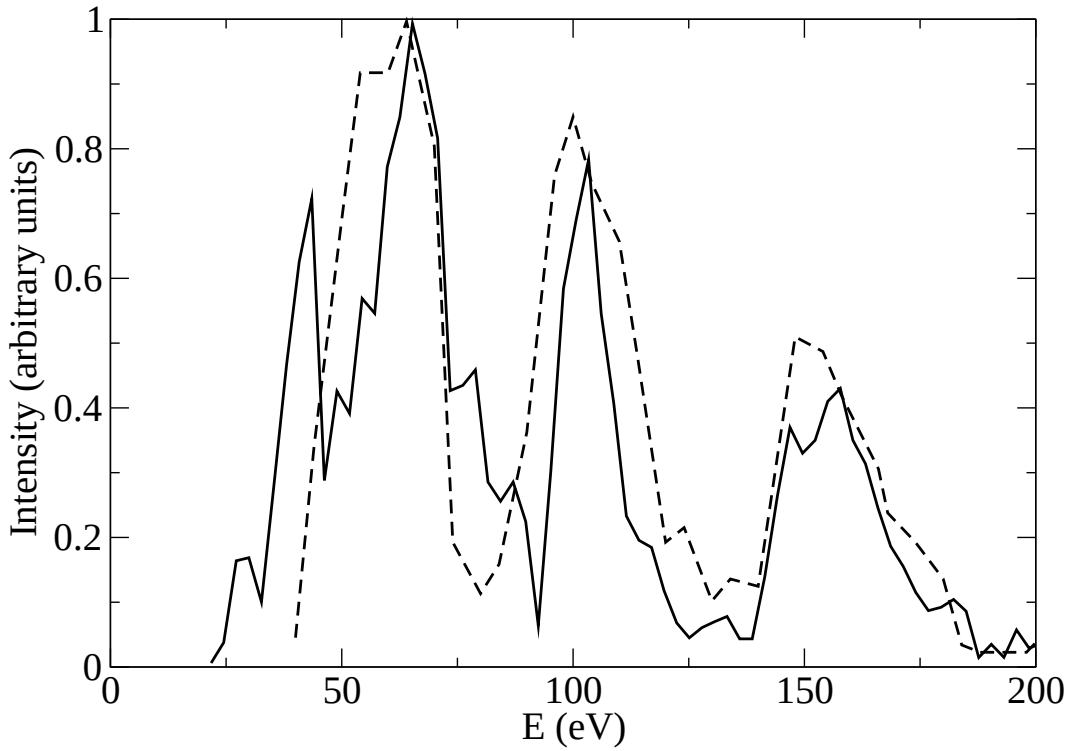

Figure 4.2: Intensity curves for diamond (111), the 1×1 surface. The solid lines are the results calculated by the present method, and the dashed lines show the results of the multislice finite difference approach [24]. This figure is reproduced from Ref. [13].

4.5 give the diffraction patterns for reflected and transmitted electrons, respectively, for several electron energies. These patterns are greatly influenced by the electron energy. This is to be expected, given the strong energy-dependence of the wavelength at low energies ($\lambda = \sqrt{150/E}$ Å) [13].

Taken together, these measurements provide strong evidence for the validity of our method; it is an intuitive computational approach that produces results in good agreement with experiment and alternative theoretical approaches. Crucially, our method can extract transmission and reflection coefficients for multiple energy points in a single calculation, greatly increasing computational efficiency. Moreover, the present

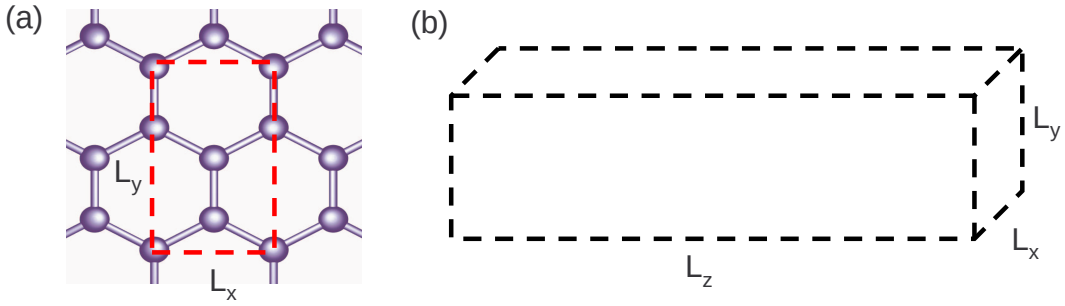

Figure 4.3: Periodic unit of a graphene lattice and a schematic of our simulation box. Measurement slices are placed on both sides of the simulation box to sample the transmitted and reflected electron densities. L_x=60 Å, L_y=2.46 Å, and L_z=$\sqrt{3}L_y$. The graphene lattice is placed at L_x=0. This figure is reproduced from Ref. [13].

approach allows for greater flexibility in the choice of potential. It is fully compatible with the muffin-tin potential, but can also accommodate all-electron potentials and pseudopotentials. However, our method must be repeated for each desired scattering direction, unlike other methods for LEED calculations. This tradeoff means that the utility of our method depends upon both the desired number of scattering angles and the desired energy range.

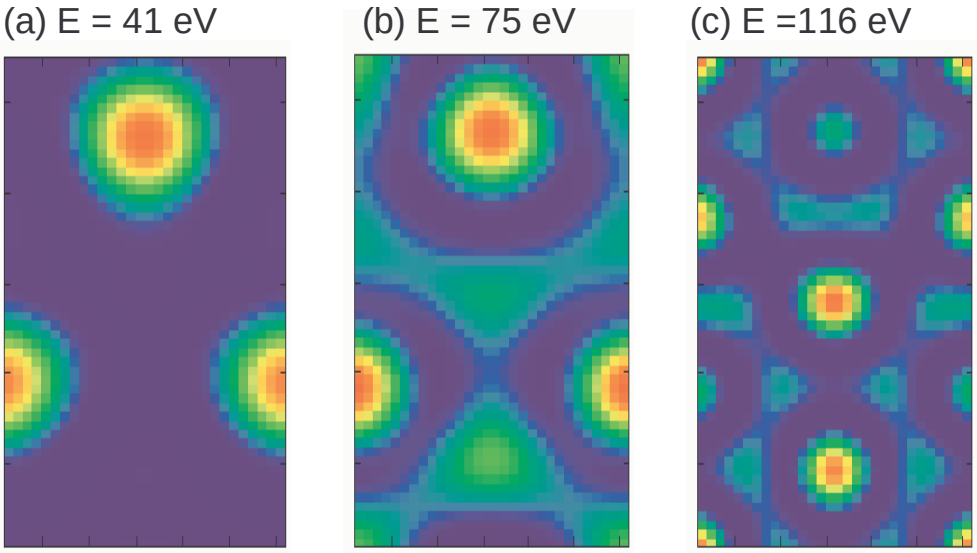

Figure 4.4: Density distribution for the reflected electron beam on the measurement slice plane, at a distance of 12.0 Å from the graphene lattice. (a) E=41 eV, (b) E=75 eV, and (c) E=116 eV. This figure is reproduced from Ref. [13].

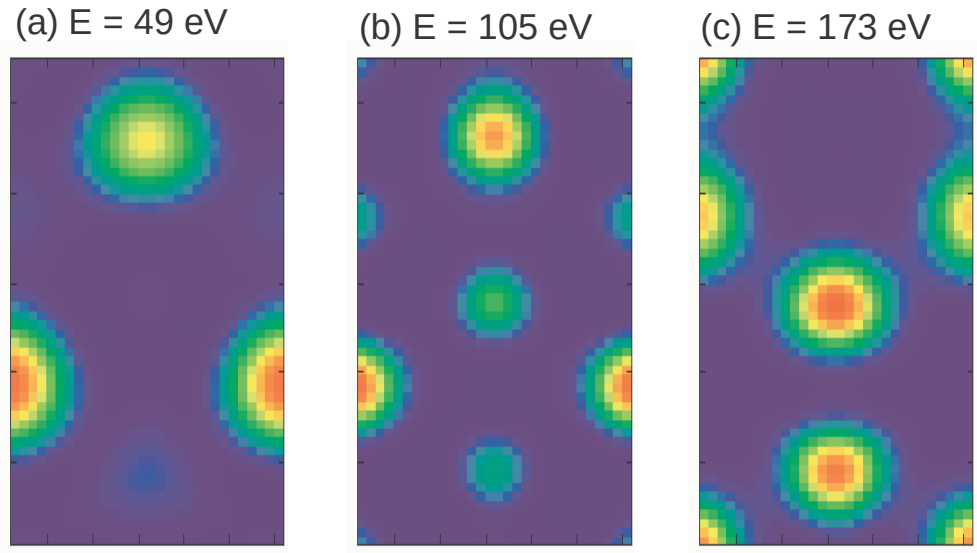

Figure 4.5: Density distribution for the transmitted electron beam on the measurement slice plane, at a distance of 12.0 Å from the graphene lattice. (a) E=49 eV, (b) E=105 eV, and (c) E=173 eV. This figure is reproduced from Ref. [13]

CHAPTER V

Attosecond Electron Pulses

5.1 Computational Setup

The fundamental idea of our attosecond 4D imaging simulations is shown in Fig. 5.1. The computational approach is very similar to the one used for LEED: an attosecond electron pulse is propagated in time, scatters from the target atom or molecule, and the electron density is recorded at the measurement plane for information about the scattering. However, several differences are worthy of mention. The most important difference is that we use DFT to calculate the electron density of our entire system, not just to model the interaction of the electron with a crystal lattice. Furthermore, since we are not interested in extracting transmission or reflection coefficients, we do not need to propagate the electron through the entire box. We need only propagate the electron until it has passed beyond the measurement plane. Moreover, since we work with the electron density for the entire calculation, there is no need to Fourier transform the wave-packet or match the electron to asymptotic

forms. We also use a single atom or molecule as the target system, rather than a crystal film, and we are interested in measuring the electron density, rather than intensity or a diffraction pattern. Our simulations use time steps of $\Delta t = 0.1$ as and grid spacings of $d = 0.125$ Å.

Our reliance on DFT is much more thorough than in our approach to LEED. We have found that this does limit the applicability of our approach to certain systems. For example, attosecond pulses are an ideal choice to image the excited states of atoms and molecules due to their short timescale relative to the oscillations of many excited systems [11]. DFT can be used to calculate the excited states of a system, but its accuracy varies greatly between systems. For example, our approach overestimates the energy of the hydrogen 2p state, resulting in an atomic orbital that is far too spatially extended to be of any use in a simulation. However, DFT does produce reasonable results for the excited states of many molecules and atoms. Nor is the DFT calculation of excited states without benefits. When we solve Eq. (3.4), we can compute the atomic orbitals of the target system. This means that our simulations work with the atomic/molecular orbitals, rather than the instantaneous (and rapidly changing) position of electrons occupying those orbitals. Therefore, when our incident attosecond electron scatters from the target system, it records information about the entire atomic orbital, rather than the instantaneous position of the bound electrons. This approach can measure the time-dependence of the orbitals without knowing the position of the individual electron at any given point in time. In this way our simulation more closely resembles an experimental scattering measurement, in which a beam of electrons is fired at the target to gain information about the orbitals, rather

than the instanteous positions of the electrons.

Before continuing to the results, some discussion of the significance of our simulations is in order. 4D imaging of electron dynamics has the potential to shed substantial light on our understanding of atomic and molecular phenomena. As described in Ref. [11], attosecond electron pulses can be used to create 4D images of charge density oscillations in excited states of atomic and molecular systems. Since the charge density is essentially constant during the scattering interaction, multiple attosecond pulses must be scattered off the target at different times during the period of charge oscillation in order to create the 4D image. We take a somewhat different approach: we wish to create 4D images of the scattering of a single electron from our target system. This allows us to better understand the dynamics of attosecond electron scattering. In particular, we can investigate how a Gaussian wave-packet is changed during the scattering process by measuring the electron density of the wave-packet before and after scattering. If the change in the wave-packet due to scattering can be characterized, then information about the target system can be gleaned from an analysis of scattered attosecond pulses.

However, due to the position of our measurement plane ($x = 5$ Å), we do not record the electron density of only the wave-packet, but the tail of the target system density as well. As such, when the electron pulse is far away from the measurement plane, we see only the electron density associated with the target. When the electron pulse is in the measurement plane, we see both its electron density and the density of the target system. By comparing these measurements, we can attempt to sort out the contributions of the electron pulse and target system to the total density. Such

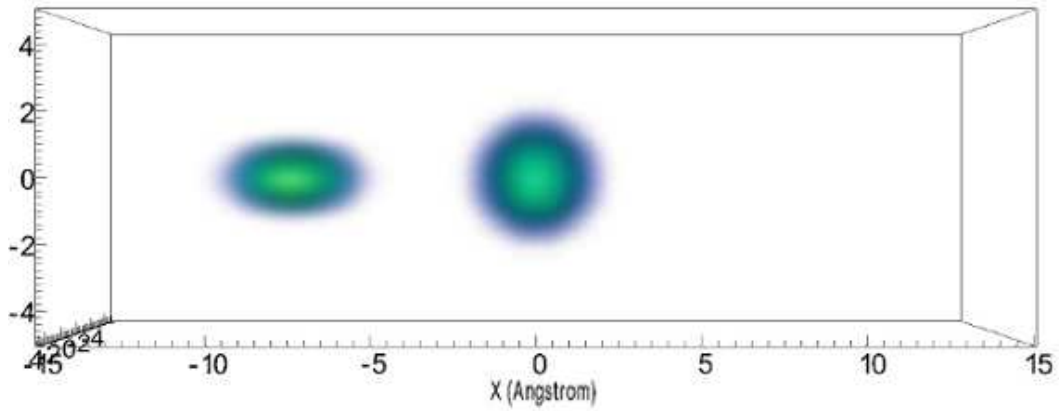

Figure 5.1: Simulation grid for attosecond electron scattering. An electron, traveling right, scatters off the target atom or molecule. A measurement plane at $x = 5$ Å records the electron density. A CAP, beginning at $x = 5$ Å, prevents reflection effects. The CAP function is very close to zero for $5x10$ Å so the wave-packet does not suffer a substantial loss of density in this region. This was confirmed through analysis of the wave-packet using Visit 2.3.0 software.

an analysis could be useful for reconstructing atomic orbitals and image correction; if the effect of the electron pulse is known, then it might be possible to remove these effects from the image, leaving only the density associated with the target system under study. This in turn should allow a more complete understanding of 4D images of atomic charge oscillations, for example, since they rely on multiple scattering processes to generate the image.

5.2 Results and Discussion

Now, we report measurements for the scattering of a 287 eV, 20 as electron pulse from the ground and first excited states of the Be atom and N_2 molecule. 4D imaging has been achieved for these systems, and are given in the Supplementary Movies. These movies record the time evolution of the electron density in the measurement

plane. The movies do not begin at the start of the time development, since the electron is very far away and does not influence the measurement plane. Rather, the movies begin when the electron is still reasonably far away from the measurement plane ($t = 80$ as), and end when the electron has passed through the measurement plane.

Here we present several representative images from the Supplementary Movies in Fig. 5.2. It is interesting to note that the attosecond electron pulse seems to cause much stronger distortions in the excited states of these systems than the ground state. Fig. 5.2(a) shows no evidence of geometric deformation; while the electron pulse does seem to concentrate the electron density in the center of the plane, resulting in a significantly smaller image of the atom, its spherical symmetry is still preserved. Fig. 5.2(c) shows some evidence of deformation, as the "hot" central core is no longer exactly spherical. It also displays a local density maxima in the intermediate region of the yz-plane, a feature not seen in any of the other simulations. Figs. 5.2(b) and (d) show significant deformities. The attosecond pulse seems to concentrate the electron density in the center of the measurement plane, giving the appearance that the atomic wavefunctions have been "pulled" towards the center.

This result implies that the attosecond electron's Gaussian form is not significantly changed by the scattering process, since most of its electron density remains concentrated in the center of the y-z plane. Given the attosecond time scale of the scattering interaction, this is not an entirely unexpected result, and it is confirmed in Fig. 5.3. The scattered wave-packet is somewhat more dispersed than its nonscattering counterpart, but both retain their Gaussian shape. This complicates applications

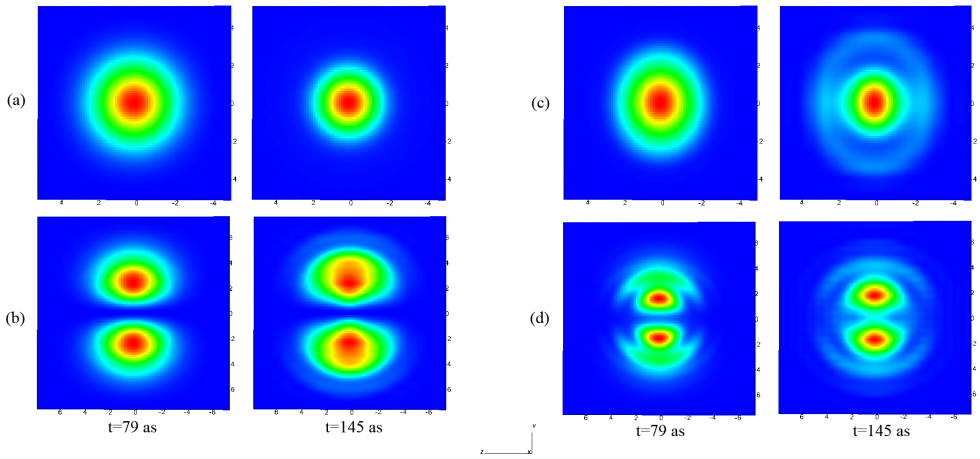

Figure 5.2: Pseudocolor plots of the electron density in the yz-plane for attosecond scattering from (a) the ground state of Be, (b) the first excited state of Be, (c) the ground state of N_2, and (d) the first excited state of N_2. The slide on the left shows the measured electron density without the influence of the attosecond electron pulse ($t = 79$ as), while the slide on the right is taken when the electron pulse is in the measurement plane ($t = 145$ as). Red represents the areas of highest electron density, blue represents the lowest electron density, etc. A larger box size was used for the excited state calculations in order to avoid reflection effects. The N_2 bond lies along the y-axis. All slides are rotated 90° from their orientation in the Supplementary Movies.

to the precise reconstruction of atomic orbitals, since the changes to the electron wave-packet due to scattering are rather subtle. On the other hand, this implies that distortions in the imaged electron density are related to the initial form of the electron wave-packet. In general, of course, the initial wave-packet is difficult to know, but some approaches to attosecond electron pulse generation can extract this information [6]. Furthermore, even if the electron's Gaussian form is largely unchanged, the supplementary movies do show some substantial differences among the systems. For example, some distortion is evident in the N_2 excited state from very close to the beginning of the movie, whereas the Be excited state does not show significant deformation until several tens of attoseconds later. More work is needed to under-

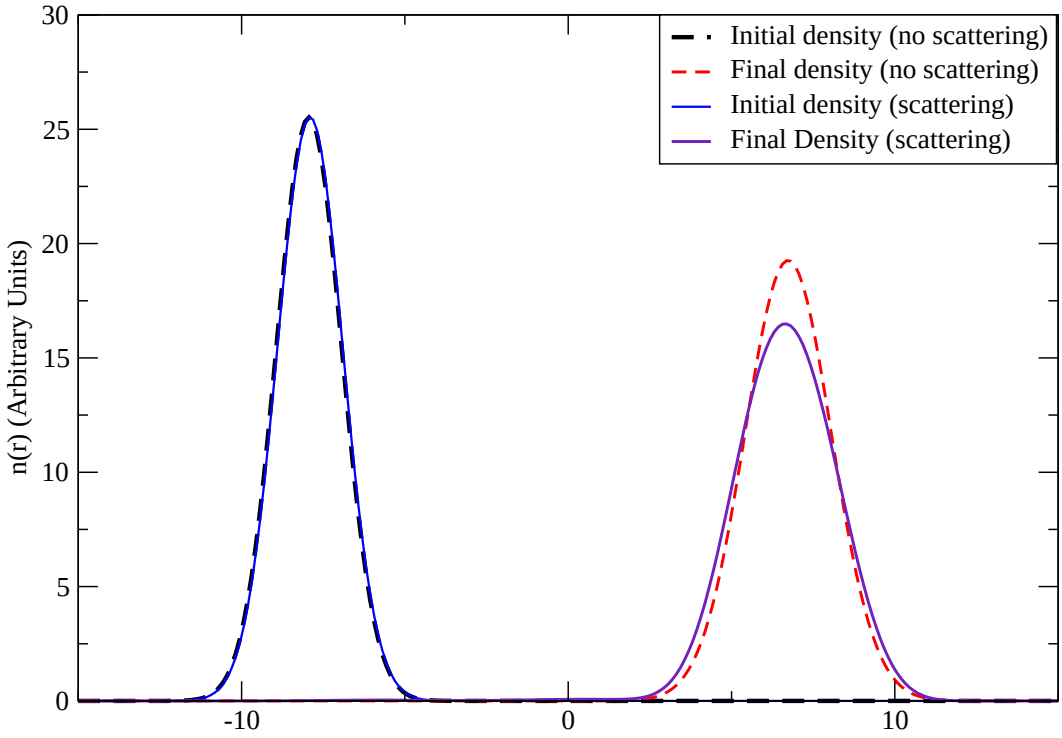

Figure 5.3: Initial and final projections of the electron density onto the x-axis for scattering (from the excited state of Be) and free-space propagation scenarios. $n(r)$ is identical for the initial cases, while the final scattering state shows evidence of greater dispersion than its nonscattering counterpart.

stand why this is the case. This is especially interesting given the small differences between the final states of the wavefunctions (see Fig. 5.4), which would seem to indicate that the scattering interactions should also be quite similar. At present, we are performing simulations with a measurement plane located farther away from the atom ($x = 9$ Å), which should allow us to view the attosecond electron pulse's density without contributions from the target system density. Once a better understanding of these phenomena is attained, our simulations could prove useful in correcting image distortions.

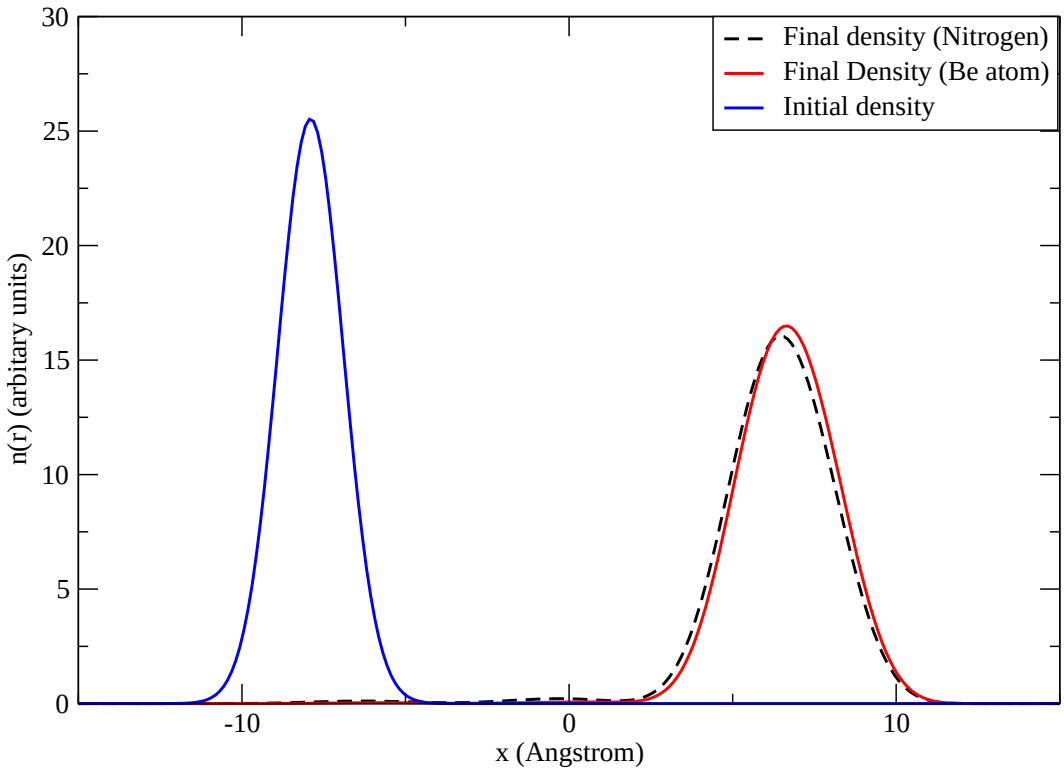

Figure 5.4: Initial and final projections of the electron density onto the x-axis for the excited states of the Be atom and N_2 molecule. The initial density distribution is identical, while there is evidence of slight differences in the final distributions.

CHAPTER VI

Conclusion

6.1 Summary

We have developed and applied real-time, real-space computational methods for two problems: the simulation of LEED measurements and the scattering of attosecond electron pulses from various atoms and molecules. We find that our method is quite useful for LEED calculations, producing results in good agreement with both experimental evidence and other theoretical approaches. Our approach to attosecond electron has successfully created "4D" images of electron scattering. While initial results suggest that the imaged density might be influenced by the form of the electron pulse, further work is needed to fully understand the scattering process. Future directions for our research include sampling of the electron density at various distances from the target system in order to further characterize the scattered wave-packet.

6.2 Acknowledgements

This work was supported in part by funds from the College Scholars Program. I thank Dr. Kalman Varga and Joseph Driscoll for their help and support throughout this project. Additionally, I thank Sergiy Bubin for many helpful discussions.

APPENDIX A

Extraction of T and R in 3D

To complete the extraction of the transmission and reflection coefficients, we follow the procedure given in Ref. [13]. In the asymptotic region, the wavefunction can be decomposed into plane waves. One needs to calculate the transmission and reflection probabilities of a plane wave with wavevector $\mathbf{k}_0$ incident on the surface of a slab of crystal. We may decompose $\mathbf{k}_0$ into components parallel and perpendicular to the direction of propagation:

$$\mathbf{k_0} = \mathbf{k_{0\parallel}} + \mathbf{k_{0\perp}} \tag{1.1}$$

When the incident wave reaches the crystal surface, part of the wavefunction will be reflected. The reflected portion will travel with wavevectors that can similarly be decomposed into parallel and perpendicular components:

$$\mathbf{k_g^-} = \mathbf{k_{g\parallel}^-} + \mathbf{k_{g\perp}^-} \tag{1.2}$$

The other part will be transmitted, with corresponding wavevectors:

$$\mathbf{k}_{\mathbf{g}}^{+} = \mathbf{k}_{\mathbf{g}\parallel}^{+} + \mathbf{k}_{\mathbf{g}\perp}^{+}. \tag{1.3}$$

Above we have used + and - to indicate transmission and reflection, respectively. From 2D momentum conservation, we obtain:

$$\mathbf{k}_{\mathbf{g}\parallel}^{+-} = \mathbf{k}_{\mathbf{0}\parallel} + \mathbf{g} \tag{1.4}$$

where $\mathbf{g}$ is the 2D reciprocal lattice vector of the crystal. To extract the transmission and reflection coefficients, we proceed by placing matching planes close to the left and right of the crystal slab (see Fig. 2.1). At points to the left of the first plane, we may write the wavefunction using the incident and reflected plane waves:

$$\Phi(\mathbf{r}, E) = e^{i\mathbf{k}_{\mathbf{0}\parallel}\cdot\rho} e^{i\mathbf{k}_{\mathbf{0}\perp}x} + \sum_{\mathbf{g}} R_{\mathbf{k}_{\mathbf{0}\perp}\mathbf{g}} e^{i(\mathbf{k}_{\mathbf{0}\parallel}+\mathbf{g})\cdot\rho} e^{-i\mathbf{k}_{\mathbf{g}\perp}^{-}x)} \tag{1.5}$$

where

$$E = \frac{\hbar^2}{2m}(\mathbf{k}_{\mathbf{0}\parallel}{}^2 + \mathbf{k}_{\mathbf{0}\perp}{}^2) \tag{1.6}$$

is the electron energy. To the right of the second matching plane, we may write the wavefunction in terms of the transmitted plane waves:

$$\Phi(\mathbf{r}, E) = \sum_{\mathbf{g}} T_{\mathbf{k}_{\mathbf{0}\perp}\mathbf{g}} e^{i(\mathbf{k}_{\mathbf{0}\parallel}+\mathbf{g})\cdot\rho} e^{i\mathbf{k}_{\mathbf{g}\perp}^{+}x} \tag{1.7}$$

Once $\Phi(\mathbf{r}, E)$ is known, one can use a Fourier transformation over the perpendicular plane (y, z):

$$\sum_{y,z} \Phi(E, \mathbf{r}) e^{-i(\mathbf{k}_{0\parallel}+\mathbf{g}\prime)\cdot\rho} = [e^{i\mathbf{k}_{\mathbf{0}\perp}x}\delta_{\mathbf{g}\prime,\mathbf{0}} + R_{\mathbf{k}_{\mathbf{0}\perp}\mathbf{g}\prime} e^{-i\bar{\mathbf{k}}_{\mathbf{g}\prime\perp}x}]N_s, \tag{1.8}$$

$$\sum_{y,z} \Phi(E, \mathbf{r}) e^{-i(\mathbf{k_0}_{\parallel}+\mathbf{g}\prime)\cdot\rho} = T_{\mathbf{k}_{\mathbf{0}\perp}\mathbf{g}\prime} e^{i\mathbf{k}_{\mathbf{g}\prime\perp}{}^{+}x} N_s, \tag{1.9}$$

where N_s is the number of surface points on our grid. With this transformation, the reflection and transmission coefficients can easily be calculated by fitting the (calculated) wavefunctions to these assumed asymptotic forms.

REFERENCES

[1] K. Heinz, Rep. Progr. Phys. **58**, 637 (1995).

[2] M. A. Van Hove, W.-H. Weinberg, and C.-M. Chan, Low-Energy Electron Diffraction (Springer, Berlin, 1986)

[3] M. De Graf, Introduction to Conventional Transmission Electron Microscopy (Cambridge University Press, Cambridge, UK, 2003).

[4] P. Goodman and A. F. Moodie, Acta Cryst. A **30**, 280 (1974).

[5] E. J. Kirkland, Advanced Computing in Electron Microscopy (Plenum, New York, 1998).

[6] P. B. Corkum and F. Krausz. Attosecond Science. Nat. Phys. 3:381-387 (2007).

[7] P. Baum and A. H. Zewail, Proc. Natl. Acad. Sci. USA **104** 47:18409-18414 (2007).

[8] T. Remetter et al. Nat. Phys. 2:323-236 (2006).

[9] Spanner, M. et al. J. Phys. B **37**, L243L250 (2004).

[10] Niikura, H. et al. Probing molecular dynamics with attoscecond resolution using correlated wave packet pairs. Nature **421**, 826829 (2003).

[11] Hua-Chieh Shao, Anthony Starace, "Detecting Electron Motion in Atoms and Molecules." Phys. Rev. Lett. **105**, 263201 (2010).

[12] D. M. Sullivan and D. S. Ditrin, J. Appl. Phy. **91**, 3219 (2002).

[13] Jia-An Yan, J.A. Driscoll, B. K. Wyatt, K. Varga, and S. T. Pantelides, "Time-Domain Simulation of Electron Diffraction in Crystals," Phys. Rev. B **84**, 224117 (2011).

[14] J. G. Muga, J. P. Palao, B. Navarro, and I. L. Egusquiza, Phys. Rep. **395**, 357 (2004).

[15] D. E. Manolopoulos, J. Chem. Phys. **117**, 9552 (2002).

[16] D. Griffiths, Introduction to Quantum Mechanics, 2nd ed. (Prentice Hall, Upper Saddle River, NJ), page 22.

[17] Kalman Varga and Joseph Driscoll, Computational Nanoscience: Applications for Molecules, Clusters, and Solids. (Cambridge University Press, Cambridge, UK), pages 11-13.

[18] Harrison, N. M., An Introduction to Density Functional Theory. Computational Materials Science, Catlow; Kotomin, Eds. IOS Press: 2003; Vol. 187.

[19] A. Beyer and A. Gölzhäuser, J. Phys.: Condens. Matter **22**, 343001 (2010).

[20] J. Y. Mutus, L. Livadaru, J. T. Robinson, R. Urban, M. H. Salomons, M. Cloutier, and R. A. Wolkow, New. J. Phys. **13**, 063011 (2011).

[21] J. R. Chelikowsky, Phys. Rev. B **21**, 3074 (1980)

[22] A. N. Kravtsova, A. V. Soldatov, M. Nachtegaal, M.W. Tew, J.A. van Bokhoven, Physica B: Condensed Matter, Volume 405, Issue 2, 15 January 2010, Pages 724-726, ISSN 0921-4526.

[23] L. G. Ferreira and J. R. Leite, Phys. Rev. A 20, 689 (1979); L. G. Ferreira, A. Fazzio, H. Closs, and L. M. Brescansin, Int. J. Quantum Chem. 16, 1021 (1979) [CAS].

[24] Huasheng Wu, Jing Wang, Ricky So, and S Y Tong, J. of Phys.: Cond Matter. **19** 386203 (2007).